Article

Gradient based optimizer with deep learning based agricultural land use and land cover classification on SAR data

Azween Abdullah[1], Daniel Arockiam[2,3,*], Valliappan Raju[4]

[1] Faculty of Applied Science and Technology, Perdana University, Kuala Lumpur 50490, Malaysia

[2] Postdoctoral Fellow, Perdana University, Kuala Lumpur 50490, Malaysia

[3] Amity University Madhya Pradesh, Gwalior 474005, India

[4] Open & Dist. Learning Centre, Perdana University, Kuala Lumpur 50490, Malaysia

* Corresponding author: Daniel Arockiam, danielarockiam@gmail.com

Abstract: Agricultural land use and land cover (LULC) classification using synthetic aperture radar (SAR) data is a fundamental application in remote sensing and precision agriculture. Leveraging the abilities of SAR, which can enter over cloud cover and deliver detailed data about surface features, allows a robust analysis of agricultural landscapes. By harnessing the control of SAR data and innovative deep learning (DL) methods, this technique provides a complete solution for effectual and automatic agricultural land classification, paving the method for informed decision-making in present farming systems. This study introduces a new gradient based optimizer with deep learning based agricultural land use and land cover classification (GBODL-ALULC) technique on SAR data. The GBODL-ALULC technique aims to detect and classify distinct types of land cover that exist in the SAR data. In the GBODL-ALULC technique, the feature extraction process takes place by a residual network with a convolutional block attention mechanism (ResNet-CBAM) model. At the same time, the GBO system has been executed for the best hyperparameter choice of the ResNet-CBAM model which helps to improve the overall LULC classification results. Finally, a regularized extreme learning machine (RELM) algorithm has been for the detection and classification of land covers. The performance study of the GBODL-ALULC method is carried out on the SAR dataset. The simulation outcome depicted that the GBODL-ALULC methodology reaches effectual LULC classification outcomes over compared methods.

Keywords: land use and land cover; synthetic aperture radar; gradient based optimizer; deep learning; residual network

1. Introduction

The agriculture sector is severely impacted by climate change, since it has an impact on both the quantity and quality of agriculture products (Fondaj et al., 2023). In recent years satellite involves in environmental research widely (Stabel and Fischer, 2001). In Agriculture industry, the heavily exploited environment must be safe for any activities connected to current agricultural production. Precision farming, which is directly related to the digitization of agriculture, is becoming more and more significant in this regard (Niedbała et al., 2023; Sánchez-Crespo et al., 2023). In recent days, the remote sensing applications can be implemented by explainable AI also (Höhl et al., 2024). Satellite remote sensing image (RSI) is utilized as a great tool to observe the surface of Earth (Allies et al., 2021), mainly in making land use and land cover (LULC) classification (Solórzano et al., 2021).

Generally, LULC classification constructs upon dual imaging methods namely microwave and optical remote sensing. Remote sensing images are widely used for analyse the wetland areas, water areas, forest areas and agriculture lands by satellite (Addison et al., 2018; Mitchard et al., 2013; Moran et al., 2004). In agriculture, the main task is trusting on an enhancement in the organization of natural resources, with knowledge permitting farming to function on a huge scale and delivering solutions that can significantly and sustainably originate a rise in farming manufacture (Mucsi et al., 2023). The on-time inventory is the need for assuring food security of agricultural regions and the local proportion of dissimilar crop kinds. The private sector contains insurance trades, and profit from early-period crop inventories as a significant element of crop manufacture estimate and farming statistics (Garg et al., 2022). Also, local estimations, and LULC mapping a vital requirement for agricultural monitoring, development, planning, digital soil mapping, creating informed policy, and resource management choices (Ngo et al., 2020). And also, LCLU mapping which helps to identify the surface heat of various land areas (Asmaa et al., 2023; Sameh et al., 2020; Sara Sameh et al., 2023). However, the manufacture of reliable and appropriate farming land cover maps utilizing optical RSI remains challenging owing to the variety and difficulty of the landscape (Kraatz et al., 2021).

Satellite RSI is suitable for land cover recognition and classification because of its high availability, wide regional coverage, and regular revisit intervals (Šćepanović et al., 2021). There are many instances of land use classification based on satellite image data on regional, local, and global scales. Previous systems with low ground resolution such as ENVISAT, SPOT, or LANDSAT were utilized for classification on a large scale with rough resolution as the Global Land Cover 2000 or CORINE project (Ajadi et al., 2021). In the present scenario, novel satellite-based multispectral scanners permitted a greater ground resolution. The classification of land use developed from this satellite information permits for a superior spatial and large difference among diverse land use classes (Vali et al., 2020). But it is old practice to map and evaluate LULC change utilizing optical satellite information, current attention has turned to the combination of optical and radar data as a more effectual model for constructing reliable forest observing methods or delivering improved data for illustrating and precisely defining land cover (Debella-Gilo et al., 2021). Uniting datasets from radar and optical sensors, which perceive dissimilar physical properties of land cover features, can deliver corresponding data across the electromagnetic spectrum and can equalize restrictions of utilizing either sensor only (Al-Dujaili, 2024). Presently, deep learning (DL) models have become another selection for land cover classification (LCC) due to their extraordinary feature removal abilities.

This study introduces a new gradient based optimizer with deep learning based agricultural land use and land cover classification (GBODL-ALULC) technique on SAR data. In the GBODL-ALULC technique, the feature extraction process takes place by the residual network with a convolutional block attention mechanism (ResNet-CBAM) model. At the same time, the GBO system is applied for the best hyperparameter range of the ResNet-CBAM model which helps to improve the overall LULC classification results. Finally, a regularized extreme learning machine

(RELM) method is useful for the recognition and classification of land covers. The simulation analysis of the GBODL-ALULC system is carried out on the SAR dataset.

2. Literature survey

Bhatt and Thakur (Bhatt et al., 2023) aim to propose an automatic DL-based LCC method of RSI. The Landsat-8 and SAR images are first pre-processed utilizing the Gabor filter method. Lastly, the features that were extracted have been exposed to improved deep belief networks (DBNs), where the weight is modified by the optimizer logic. Due to this, a novel sunflower adopted red deer (SARD) model has been presented that combines the idea of a Sunflower optimizer and Red Deer model. In the study of Jang et al. (2023), a management system for SAR images is developed. Consumers can generate their classifier by using their information, and get the classified outcomes of afresh SAR images. The classifier is dependent upon the convolutional neural network (CNN) structure. In the study of Darvishnezhad et al., (2023), a new self-supervised ensemble learning framework (SSELF) is planned. This model can mechanically remove features to the classification of polarimetric SAR (PolSAR) images with a small amount of training samples.

In the study of Wu et al. (2022), cross-channel reconstruction (CCR-Net) is able to develop more compact fusion representation of remote sensing (RS) data sources and share information among them efficiently. In the study of Hosseiny et al. (2022), uses satellite information and ensemble deep learning model to create a classification for mapping wetland areas.

In the study of Hosseiny et al. (2024), proceeded with the develop of nonsupervised deep learning (NSDL) models for various remote sensing applications. Di Martino et al. (2023) develop FARMSAR: Fixing AgRicultural Mislabels Using Sentinel-1 Time Series and AutoencodeRs to scale and present the suitable crop for farmers using temporally dense Sentinel-1 data and class-specific convolutional autoencoders applied to synthetic aperture radar (SAR) time series.

In the research of Huang et al. (2023), an enhanced dual-pol radar vegetation index built on many mechanisms (DpRVIm) and an innovative LCC model have been developed. At first, the scattering data and territory factors were measured to increase the separability. Then, the 1D-CNN model is utilized to examine the outcome of dissimilarity DpRV indexes on LCC. Lastly, to decrease the outcome of the speckle noise, a dual-stage LCC model based on 1DCNN- Markov Random Field (1DCNN- MRF) was projected by considering the spatial data of the ground object. Dahhani et al. (2022) directed to map the LULC, particularly in farming regions, utilizing SAR C-band Sentinel-1 (S-1) time sequence. The author measured the processing time and performance of 3 machine learning (ML) classifiers on dual inputs. Lapini et al. (2020) define a field mapping study in a settled region in Tuscany (Italy). The S-1 C-band, S-2 optical sensors, and Constellation of Small Satellites for Mediterranean basin Observation-SkyMed (COSMO-SkyMed) are classifiers input.

In the study of Hosseiny et al. (2022), compared three shallow learners and two deep learners by different machine learning approaches using sentinel 2 satellite.

Explored various deep learning architectures on RS image processing and attention mechanism-based deep learning (At-DL) methods for improving accuracy on RS image processing (Ghaffarian et al., 2021).

Chatterjee et al. (2021) developed a semi-supervised model that identifies paddy fields in numerous periods. The method has been separated into dual parts such as supervised and unsupervised. The visual geometry group 16 (VGG16) technique is employed to separate areas into 5 groups. Chatterjee et al. (2020) project an unsupervised learning model to cluster dual-polarized and hybrid polarimetric SAR images utilizing the deep framework. The author employs the VGG16 method with batch normalization that is trained by tiny covers delivered from the hybrid polarimetric SAR image.

3. The proposed method

In this research, we have developed an innovative GBODL-ALULC method for SAR data. The GBODL-ALULC technique aims to detect and classify distinct types of land cover that exist in the SAR data. The GBODL-ALULC technique compresses three distinct processes namely ResNet-CBAM-based feature extraction, GBO-based hyperparameter tuning, and RELM-based classification process. **Figure 1** illustrates the entire flow of the GBODL-ALULC technique.
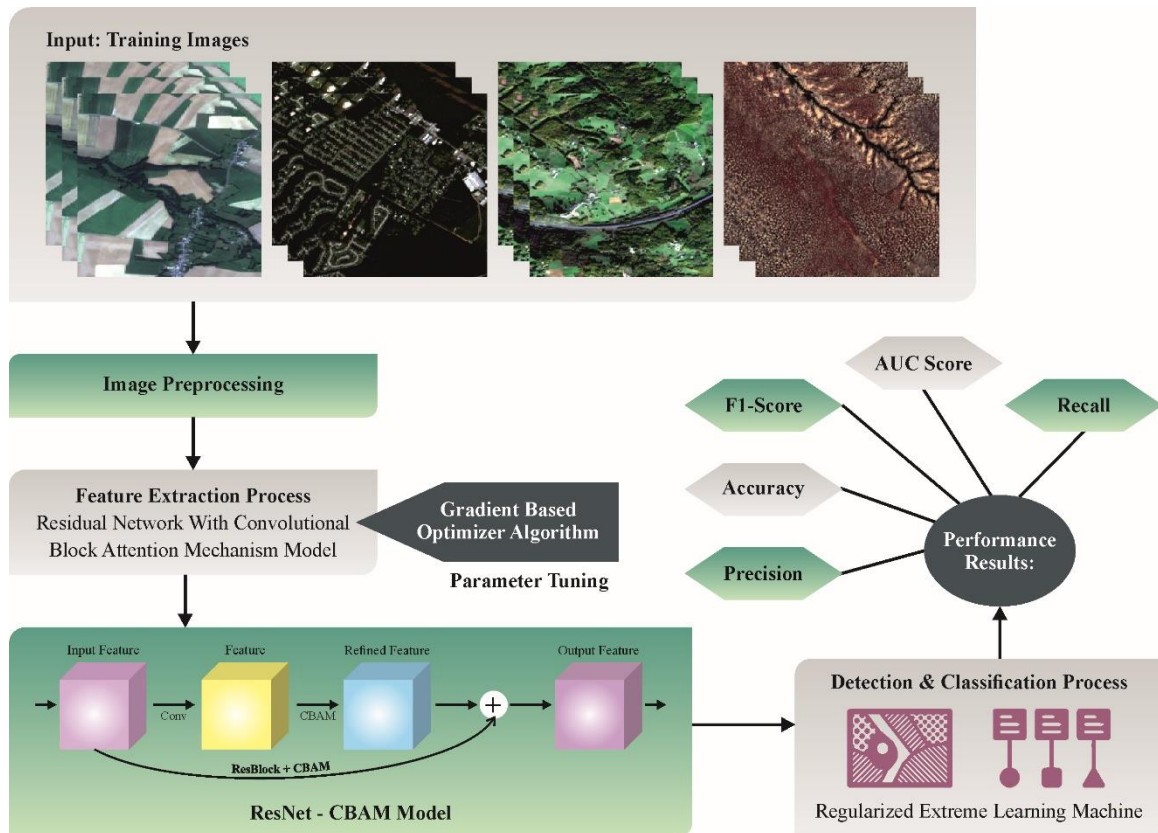

Figure 1. Overall flow of GBODL-ALULC technique.

3.1. ResNet-CBAM-based feature extraction

In the GBODL-ALULC technique, the feature extraction process takes place by the ResNet-CBAM model. Deep neural networks (DNN) have many layers of

convolutional (Conv) and pooling to remove features (Wang, 2024). A ResNet is a kind of traditional CNN that employs the design of residual as the foremost form to prevent gradient disappearance.

$$H(x) = F(x) + x \tag{1}$$

In Equation (1), $F(x)$ denotes the straight mapping of the input x.

The residual block (RB) utilizes the jump connection model to remove features but hold a fragment of the unique input data. The learning aim of residual is 0 to decrease the dissimilarity between output and input. The RB structure has dual equal output channels of three 3×3 Conv layers; every Conv layer is linked with an activation function of rectified linear unit (ReLu) and batch normalized (BN) layer. The input and output forms of the dual Conv layer must be reliable so that they can be covered.

In the feature extractor phase of NN, the amount of fault samples is lesser than regular samples. Therefore, the removal of the fault feature parameter is inadequate. The feature extractor phase in CBAM is inserted into NN models and can resolve issues like lower model accuracy and weak simplification owing to inadequate extractor capability for feature parameters. Enlarging the usage of restricted fault samples is significant in dealing with imbalanced issues. We propose an enhanced Conv residual network and insert the attention mechanism of Conv in every RB structure. Throughout the feature extractor phase, the feature plan is highlighted; then, with the aid of a spatial attention device, the system can focus on valuable feature data. Besides, this connection safeguards that the system acquires more deep features while preserving performance. So, the convergence of the network is enhanced, and classification of high accuracy is attained.

Simultaneously, the RB structure employs the BN layer. The ReLu is employed to attach Conv layers, increase the training speed and generalized capability, and diminish the issue of over-fitting.

3.2. Hyperparameter tuning using the GBO model

At this stage, the GBO model is applied for the best hyperparameter range of the ResNet-CBAM model which helps to improve the overall LULC classification results. An advanced metaheuristic technique termed the GBO algorithm integrates gradient-based and population-based methods (Manderna et al., 2023). It proficiently discovers full search space by employing an assortment of vectors as well as dual operations. GBO pursues to determine the finest solutions for an assumed set of exploration metrics by replicating gradient-based, population-based, and Newtonian techniques.

Initialization:

At the time of initialization, the GBO method employs probability rate (β) and control parameters (α) to equilibrium among exploration and exploitation. The iterations count and extent of populace altered affording to the difficulty of problematic being cracked. In an algorithm of GBO, solution space is signified by N. The early vectors are produced arbitrarily in the search space that is given in Equation (2).

$$x_n = x_{\min} + r(0,1) \times (x_{\max} - x_{\min}) \tag{2}$$

whereas $r(0,1)$ signifies a random amount within ranges of $[0,1]$, and $x_{\min}$ and $x_{\max}$ represent lower and upper bounds of decision variable x, singly.

Gradient search rule (GSR):

The GBO model employs a main module to attain a stable exploration of significant search space areas while attaining global as well as optimum spots. The use of ρ defined in Equations (3)–(5).

$$\rho 1 = 2 \times r \times \alpha - \alpha \tag{3}$$

$$\alpha = \left| \beta \times \sin\left(\frac{3\pi}{2}\right) + \sin\left(\beta \times \frac{3\pi}{2}\right) \right| \tag{4}$$

$$\beta = \beta_{\min} + (\beta_{\max} - \beta_{\min}) \times ((1 - c/T)^3)^2 \tag{5}$$

where, $\beta_{\min}$ and $\beta_{\max}$ denote a constant value of 0.2 and 1.2, correspondingly, T signifies the entire number of iterations, and c refers to current iterations. Depending on the function of sine, parameter $\rho 1$ is responsible for balancing exploitation and exploration. It varies enthusiastically through optimization procedure creation with a great value to stimulate a huge array of solutions and gradually drop over iterations to accelerate convergence. The technique efficiently examines a large extent of substitute solution by enhancing parameter value over identified iterations within range. This methodology improves the GBO model's capability to professionally search as well as discover optimum solutions while preserving a balance among exploration as well as exploitation. Global search radius (*gsr*) is considered by utilizing Equation (6).

$$gsr = r \times \rho 1 \times 2 \Delta x \times \frac{x_n}{x_{\text{worst}} - x_{\text{best}} + \varepsilon} \tag{6}$$

Random performance is used to generate a randomized exploration device that simplifies the finding of local goals. The variable Δx alterations are presented by Equations (7) and (9). A random number (r) is presented to permit exploration.

$$\Delta x = r(1:N) \times |\text{step}| \tag{7}$$

$$\text{Step} = (x_{\text{best}} - x_{r1}^c)/2 + \delta/2 \tag{8}$$

$$\delta = 2 \times r \times \left| x_{r1}^c + x_{r2}^c + x_{r3}^c + \frac{x_{r4}^c}{4} - x_n^c \right| \tag{9}$$

whereas, $r(1:N)s$ signifies a random vector in the range of $[0 \text{ and } 1]$. The *gsr* computation combines these random factors to help a familiar exploration procedure that permits the GBO technique to successfully discover possible solutions with local targets in search space. 4 self-governing integers ($r1, r2, r3, \text{and } r4$) arbitrarily selected in GBO procedure so ($r1 \neq r2 \neq r3 \neq r4 \neq n$). The dissimilarity between x_{best} and x_{r1}^c attends as an amount of stage scale that step signifies as revealed in Equation (8). Direction movement (*dm*) is employed to effort vectors (*x*) near convergence through the solution field in order to get convergence. *dm* presented to move x_n in the way of optimal vector ($x_{\text{best}} - x_n$) and calculated according to Equation (10).

$$dm = r \times \rho 2 \times (x_{\text{best}} - x_n) \tag{10}$$

whereas, $\rho 2$ denotes an arbitrary parameter that is used to alter the stage size. r represents evenly distributed value in ranges of $[0,1]$. $\rho 2$ intended by Equation (11).

$$\rho 2 = 2 \times r \times \alpha - \alpha \tag{11}$$

Equations (12) and (13) are modified by *gsr* and *dm* since the current vector is

denoted as x_n^c.

$$x1_n^c = x_n^c - gsr + dm \tag{12}$$

where $x1_n^c$ signifies the modified vector resultant from alterations complete to $x1_n^c$. The transformation of $x1_n^c$ is conveyed as per Equation (13).

$$x1_n^c = x_n^c - r \times \rho1 \times \frac{2\Delta x \times x_n^c}{(vp_n^c - vq_n^c + \varepsilon)} + r \times \rho2 \times (x_{\text{best}} - x_n^c) \tag{13}$$

while, vp_n^c, vq_n^c resemble $v_n + \Delta x$ and $v_n - \Delta x$, correspondingly. The vector v_n is the average of dual vectors i.e., x_n and Z_{n+1} in Equation (14).

$$Z_{n+1} = x_n - r \times (2\Delta x \times x_n)/x_{\text{worst}} - x_{\text{best}} + \varepsilon) \tag{14}$$

Equation (15) is employed to enhance local search exploitation as well as global search at the time of finding procedure. By replacing the present solution vector x_n^c with novel solution vector x_{best}, the current solution vector $x2_n^c$ is gained:

$$x2_n^c = x_{\text{best}} - r \times \rho1 \times \frac{2\Delta x \times x_n^c}{(vp_n^c - vq_n^c + \varepsilon)} + r \times \rho2 \times (x_{r1}^c - x_{r2}^c) \tag{15}$$

Then, a novel version of the solution x_n^{c+1} is computed by Equation (16).

$$x_n^{c+1} = ra \times (rb \times x1_n^c + (1 - rb) \times x2_n^c) + (1 - ra) \times x3_n^c \tag{16}$$

whereas ra and rb denote random numbers within ranges of [0 and 1], and $x3_n^c$ defined by Equation (17).

$$x3_n^c = x_n^{c+1} - \rho1 \times (x2_n^c - x1_n^c) \tag{17}$$

The local escaping operator (LEO) procedure is an effective model employed in the optimizer procedure to overwhelm local optima and improve convergence. LEO aids procedures in quickly transferring away from sub-optimal solutions as well as discovering novel areas of search space. By including LEO, the optimizer model attains the capability to discover superior as well as more effectual solutions. This operation plays a vital part in enhancing the performance and efficiency of optimizer models and makes them stronger for resolving difficult optimization challenges.

The fitness function (FF) is the significant factor that influences GBO model performance. The hyperparameter range procedure contains the solution encode technique to calculate the efficiency of the candidate solution. In this study, the GBO model takes accuracy as the main measure to plan the FF as conveyed below.

$$\text{Fitness} = \max(P) \tag{18}$$

$$P = \frac{TP}{TP + FP} \tag{19}$$

here, FP and TP denote the false and true positive values in Equations (18) and (19).

3.3. Detection using the RELM model

At last, the RELM method is applied for the detection and classification of land covers. As an improved SLFN, ELM presents M training samples (Li, 2024). **Figure 2** defines the infrastructure of ELM.

$\{(x_j, t_j), j = 1, \cdots, M\}, x_j = \{x_1, x_2, \cdots, x_m\}^T, t_j = \{t_1, t_2, \cdots, t_n\}^T, x_j, t_j$ indicate the input vector and output vectors of j-th samples, correspondingly. The activation function is (w, b, x), and the HL node is set as L and t, the architecture of ELM comprises n output neurons, m input neurons, and L hidden neurons:

$$t_j = \sum_{i=1}^{L} \beta_i g_i(w_i \cdot x_j + b_i) j = 1, \cdots, M \tag{20}$$

In Equation (20), $\beta_i = [\beta_{i1}, \beta_2 l, \cdots, \beta_{iL}]^T$ shows the connecting weight vector of i-th hidden neurons to the output layer, $W_i = \{W_{i1}, W_2 l, \cdots, W_{iL}\}^T$ signifies the connecting weight vector of i-th hidden neurons to the input layer, X_j represents features, and b_i represents the bias of i-th hidden nodes, each of them is produced at random.

$$T = H\beta \tag{21}$$

$$H = \begin{pmatrix} g(\omega_1, b_1, x_1) & g(\omega_2, b_2, x_1) & ... & g(\omega_L, b_L, x_1) \\ g(\omega_1, b_1, x_2) & g(\omega_2, b_2, x_2) & ... & g(\omega_L, b_L, x_2) \\ \vdots & \vdots & \vdots & \vdots \\ g(\omega_1, b_1, x_N) & g(\omega_2, b_2, x_N) & ... & g(\omega_L, b_L, x_2) \end{pmatrix} \tag{22}$$

Equation (22) is substituted to Equation (21) and is attained Equation (23) by singular value and least square decomposition:
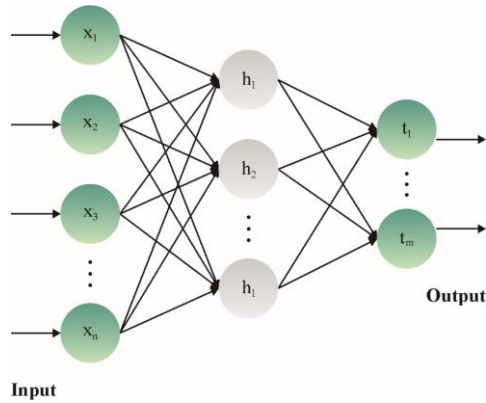
$$\beta = (H^T H)^{-1} H^T T \tag{23}$$

Figure 2. Architecture of ELM.

The regularization coefficient enhances the structural stability of ELM and produces RELM:

$$\beta = (H^T H + CI)^{-1} H^T T \tag{24}$$

In Equation (24), I shows the unit matrix and C indicates the regularization factor.

4. Performance validation

The SAR data analysis of the GBODL-ALULC technique for LULC classification takes place on Sentinel-12 data from the Kaggle repository (https://www.kaggle.com/datasets/requiemonk/sentinel12-image-pairs-segregated-by-terrain). The database comprises 16,000 samples with 4 classes as illustrated in **Table 1**. **Figure 3** depicts the sample images.

Table 1. Details of the dataset.

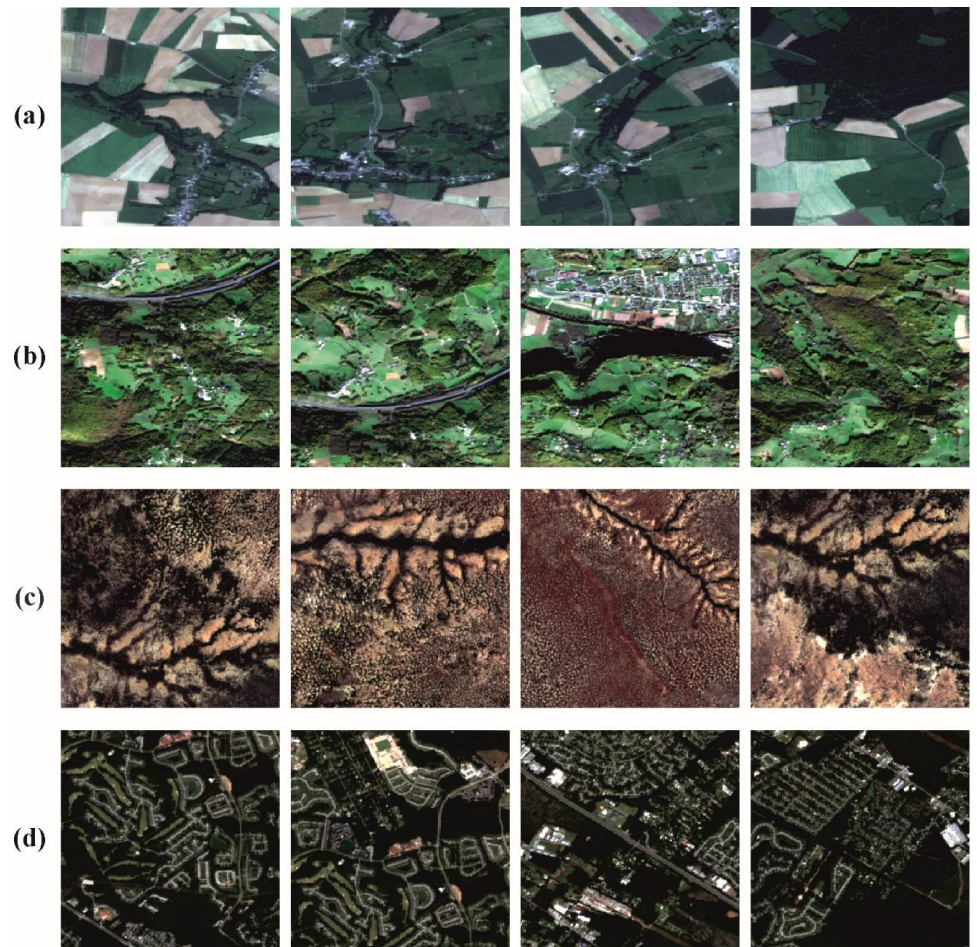| Classes	No. of instances
Barren land	4000
Grassland	4000
Agricultural land	4000
Urban areas	4000
Total samples	**16,000**

Figure 3. Sample images: **(a)** barren land; **(b)** grassland; **(c)** agricultural land; **(d)** urban areas.

Figure 4 illustrates the confusion matrices accomplished by the GBODL-ALULC method with 80:20 and 70:30 of TRAPH/TESPH. These results represent the proficient recognition with four samples under every class.

The LULC detection results of the GBODL-ALULC method with 80:20 of TRAPH/TESPH are given in **Table 2** and **Figure 5**. These achieved outcomes imply the proficient performance of the GBODL-ALULC system under all classes. According to 80% of TRAPH, the GBODL-ALULC method gives an average $accu_y$ of 97.52%, $prec_n$ of 95.09%, $reca_l$ of 95.05%, F_{score} of 95.05%, and $G_{measure}$ of 95.06%. Meanwhile, based on 20% of TESPH, the GBODL-ALULC approach gains an average $accu_y$ of 97.39%, $prec_n$ of 94.83%, $reca_l$ of 94.78%, F_{score} of 94.79%, and $G_{measure}$ of 94.79%, respectively.
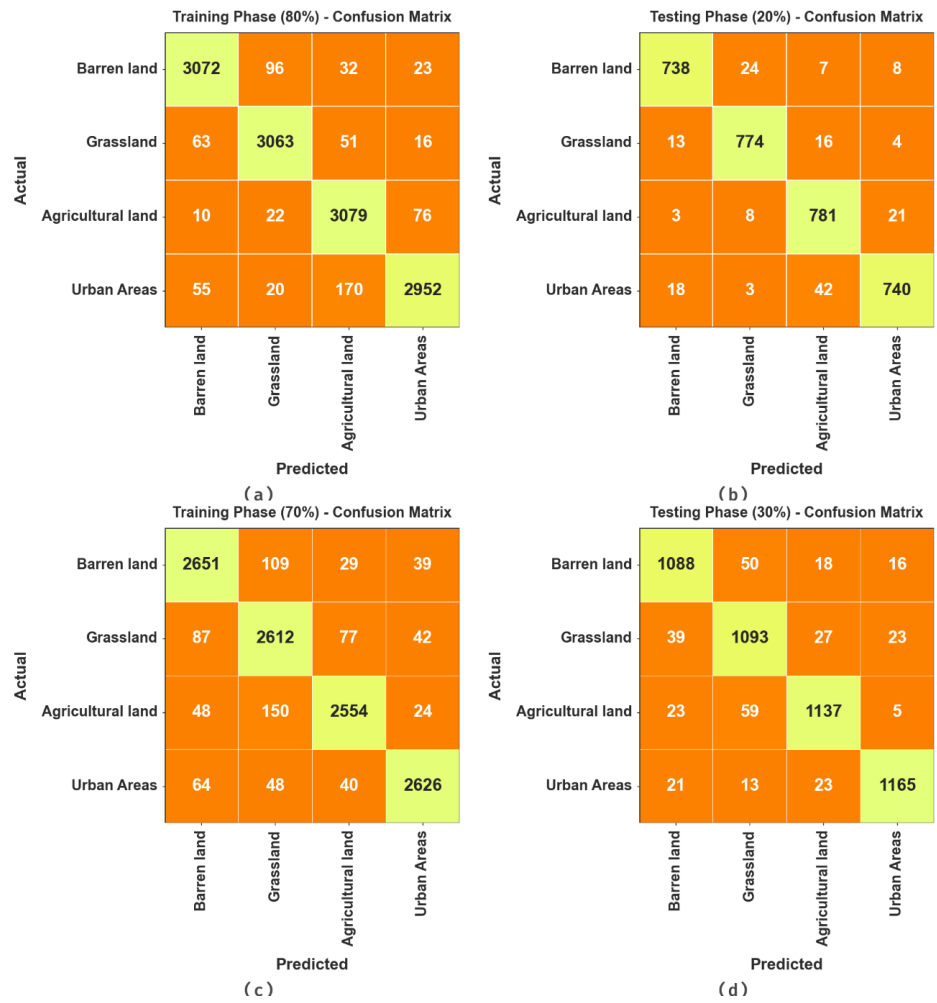
Figure 4. Confusion matrices of the GBODL-ALULC model under **(a)** and **(b)** 80:20 TRAPH/TESPH; and **(c)** and **(d)** 70:30 TRAPH/TESPH.

Table 2. LULC detection results of the GBODL-ALULC algorithm on 80:20 of TRAPH/TESPH.

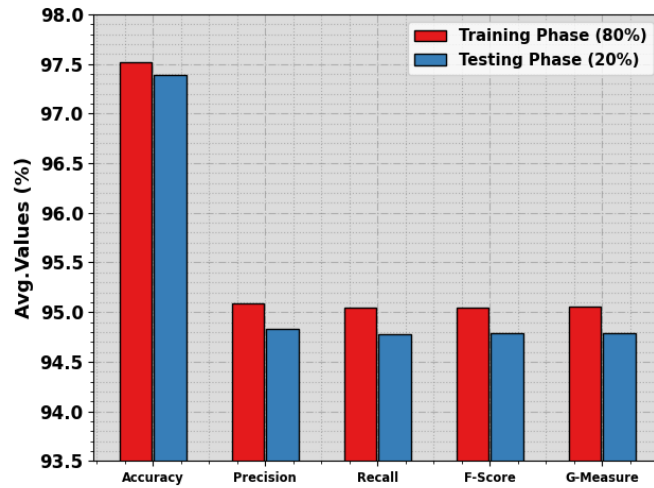| Classes	$Accu_y$	$Prec_n$	$Reca_l$	F_{score}	$G_{measure}$
TRAPH (80%)					
Barren land	97.82	96.00	95.31	95.66	95.66
Grassland	97.91	95.69	95.93	95.81	95.81
Agricultural land	97.18	92.41	96.61	94.46	94.49
Urban Areas	97.19	96.25	92.34	94.25	94.27
Average	**97.52**	**95.09**	**95.05**	**95.05**	**95.06**
TESPH (20%)					
Barren land	97.72	95.60	94.98	95.29	95.29
Grassland	97.88	95.67	95.91	95.79	95.79
Agricultural land	96.97	92.32	96.06	94.15	94.17
Urban areas	97.00	95.73	92.15	93.91	93.93
Average	**97.39**	**94.83**	**94.78**	**94.79**	**94.79**

Figure 5. Average of the GBODL-ALULC method with 80:20 of TRAPH/TESPH.

Table 3. LULC detection outcomes of the GBODL-ALULC model at 70:30 of TRAPH/TESPH.

| Classes	$Accu_y$	$Prec_n$	$Reca_l$	F_{score}	$G_{measure}$
TRAPH (70%)					
Barren land	96.64	93.02	93.74	93.38	93.38
Grassland	95.42	89.48	92.69	91.06	91.07
Agricultural land	96.71	94.59	92.00	93.28	93.29
Urban areas	97.71	96.16	94.53	95.33	95.34
Average	**96.62**	**93.31**	**93.24**	**93.26**	**93.27**
TESPH (30%)					
Barren land	96.52	92.91	92.83	92.87	92.87
Grassland	95.60	89.96	92.47	91.20	91.21
Agricultural land	96.77	94.36	92.89	93.62	93.62
Urban areas	97.90	96.36	95.34	95.85	95.85
Average	**96.70**	**93.40**	**93.38**	**93.38**	**93.39**
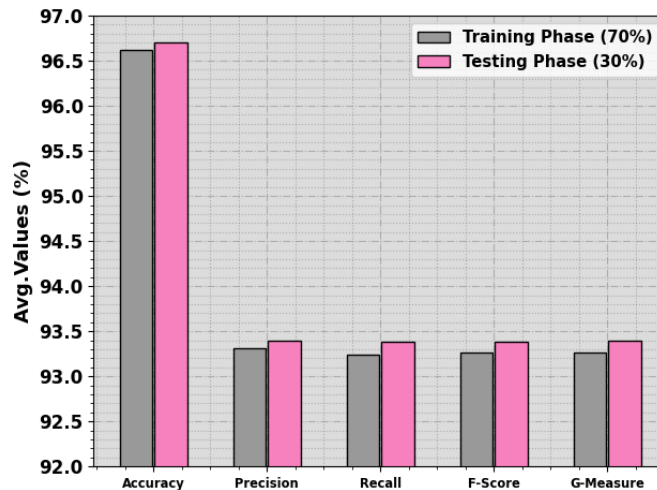
Figure 6. Average of the GBODL-ALULC algorithm with 70:30 of TRAPH/TESPH.

The LULC detection results of the GBODL-ALULC algorithm with 70:30 of TRAPH/TESPH can be reported in **Table 3** and **Figure 6**. These accomplished findings imply the proficient performance of the GBODL-ALULC system under each class. According to 70% of TRAPH, the GBODL-ALULC method provides an average $accu_y$ of 96.62%, $prec_n$ of 93.31%, $reca_l$ of 93.24%, F_{score} of 93.26%, and G_{measure} of 93.27%. Additionally, with 30% of TESPH, the GBODL-ALULC algorithm obtained an average $accu_y$ of 96.70%, $prec_n$ of 93.40%, $reca_l$ of 93.38%, F_{score} of 93.38%, and G_{measure} of 93.39%.
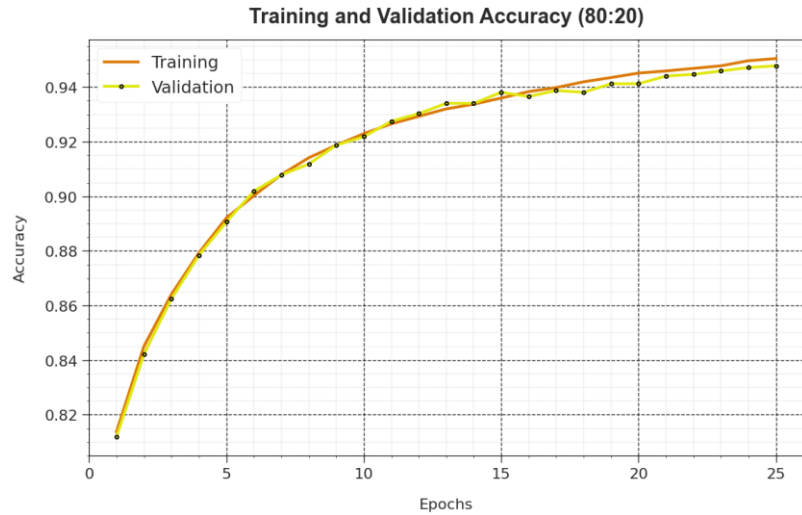

Figure 7. $Accu_y$ curve of the GBODL-ALULC model with 80:20 of TRAPH/TESPH.

The $accu_y$ curves for training (TRA) and validation (VL) demonstrated in **Figure 7** for the GBODL-ALULC algorithm with 80:20 of TRAPH/TESPH provides valued insights into its efficiency at multiple epochs. Generally, it can be an incessant upgrading under the TRA and TES $accu_y$ with increased epochs, proving the proficiencies of the model for learnable and recognizable patterns with the TRA and TES data. The higher trends in TES $accu_y$ underscores the model's adaptabilities to the TRA dataset and the ability to produce detailed predictions on unnoticed data, emphasizing capabilities of robust generalization.

Figure 8 illustrates an extensive result of the TRA and TES loss values for the GBODL-ALULC method at 80:20 of TRAPH/TESPH in varying epochs. The TRA loss continually lessened as a model refines the weights for diminishing classification errors at both datasets. The loss curves prominently show the alignments with the TRA data, accentuating the ability to capture patterns successfully. Significant can be the persistent upgrading of parameters in the GBODL-ALULC technique, targeted at lessened differences between actual and TRA prediction labels.
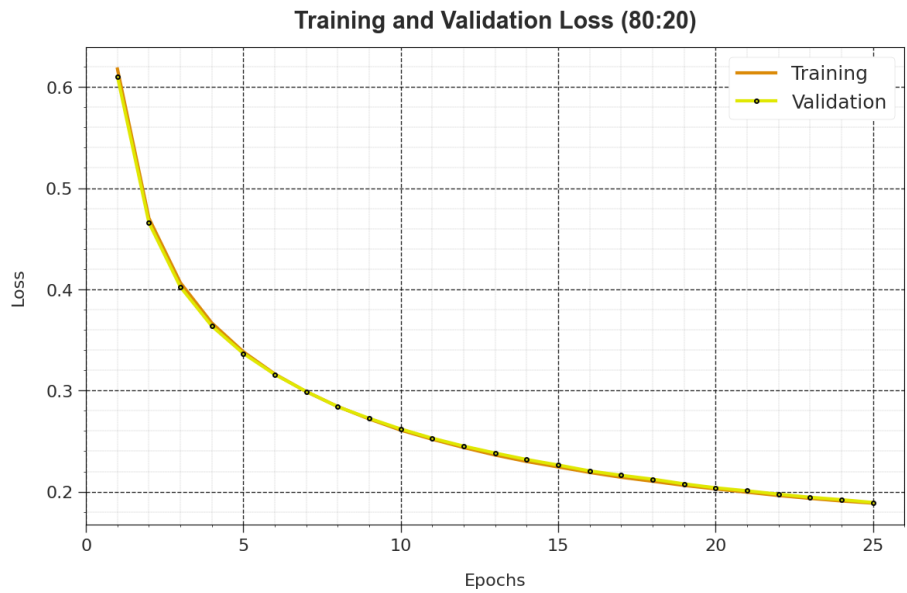
Figure 8. Loss curve of the GBODL-ALULC technique at 80:20 of TRAPH/TESPH.
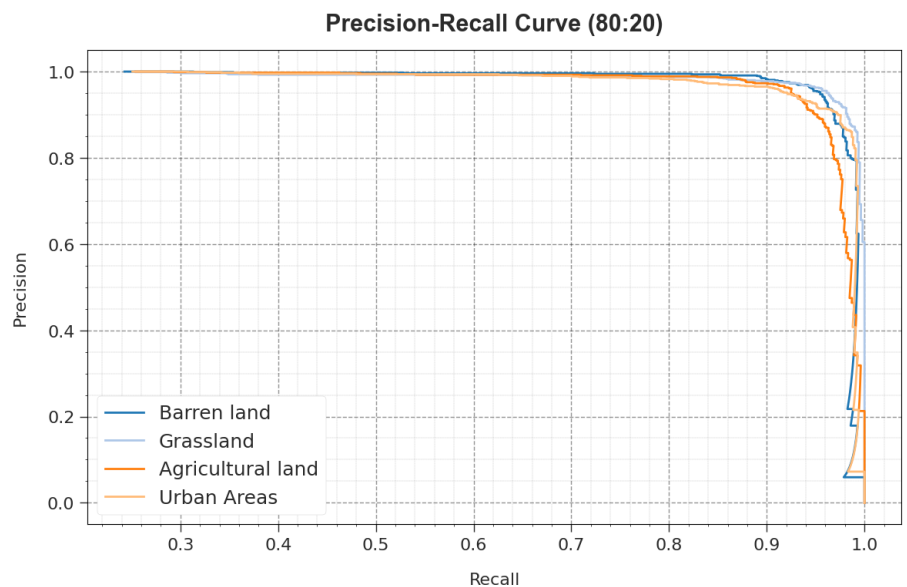

Figure 9. PR curve of the GBODL-ALULC model with 80:20 of TRAPH/TESPH.

As regards the PR curve displayed in **Figure 9**, the findings clearly affirm that the GBODL-ALULC method with 80:20 of TRAPH/TESPH continuously accomplishes higher PR values in every class. These outcomes underscore the efficient capacity of the model for discriminating between numerous classes, emphasizing its effectiveness in exactly recognizing class labels.

Similarly, in **Figure 10**, we present ROC curves made by the GBODL-ALULC algorithm with 80:20 of TRAPH/TESPH, representing its proficiency in distinguishing between classes. These curves provide valuable insights into how the trade-off among FPR and TPR changes in multiple classification epochs and thresholds. The results underscore the model's precise classification efficiency in diverse class labels, underscoring its effectiveness in addressing many classification challenges.
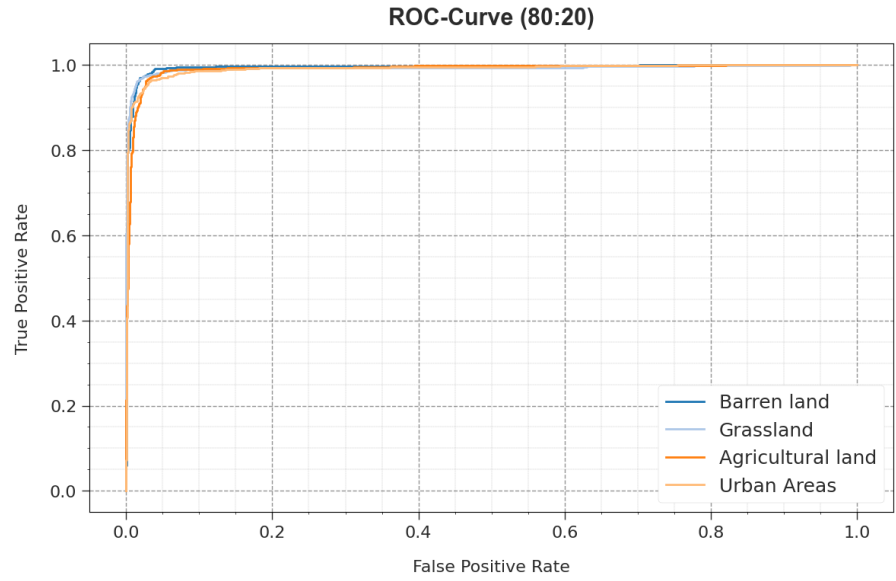
Figure 10. ROC curve of the GBODL-ALULC system at 80:20 of TRAPH/TESPH.

Table 4. Comparative results of the GBODL-ALULC system with other algorithms.

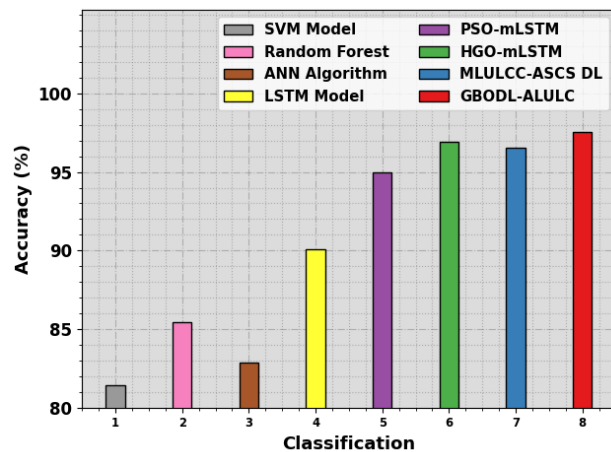| Classification	$Accu_y$	$Prec_n$	$Reca_l$	F_{score}
SVM model	81.45	72.33	78.80	77.24
Random forest	85.44	75.85	72.30	73.22
ANN algorithm	82.84	70.33	70.51	73.05
LSTM Model	90.09	91.38	92.91	92.59
PSO-mLSTM	95.00	92.00	93.98	92.91
HGO-mLSTM	96.90	94.50	94.00	92.49
MLULCC-ASCS DL	96.51	92.99	92.59	92.81
GBODL-ALULC	97.52	95.09	95.05	95.05

Figure 11. $Accu_y$ outcome of GBODL-ALULC model compared with other systems.

To represent the superior performance of the GBODL-ALULC system, a wide range of comparison studies is given in **Table 4** (Arrechea-Castillo, 2023; Stateczny, 2022). **Figure 11** illustrates the comparative results of the GBODL-ALULC technique in terms of $accu_y$. Based on $accu_y$, the GBODL-ALULC technique offers

increased $accu_y$ of 97.52% whereas the SVM, RF, ANN, LSTM, PSO-mLSTM, HGO-mLSTM, and MLULCC-ASCS DL systems reported reduced $accu_y$ values of 81.45%, 85.44%, 82.48%, 90.09%, 95.00%, 96.90%, and 96.51%, respectively.
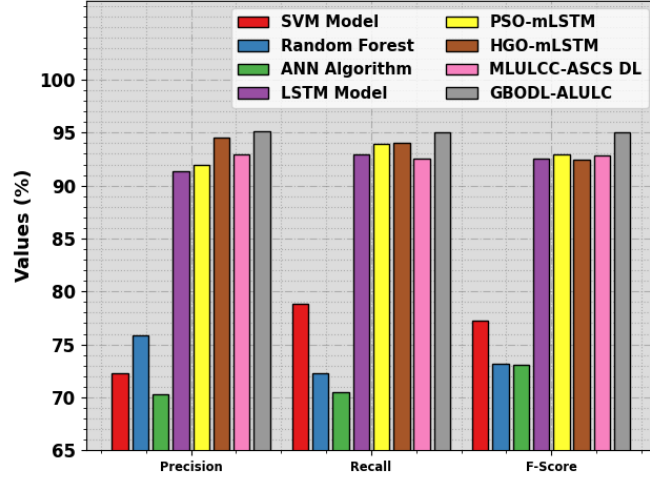

Figure 12. $Prec_n$, $reca_l$, and F_{score} outcome of GBODL-ALULC technique compared with other algorithms.

To display the excellent performance of the GBODL-ALULC system, an extensive comparison analysis can be described in **Figure 12** shows the comparative results of the GBODL-ALULC method with respect to $prec_n$, $reca_l$, F_{score}. According to $prec_n$, the GBODL-ALULC algorithm gets an increased $prec_n$ of 95.09% whereas the SVM, RF, ANN, LSTM, PSO-mLSTM, HGO-mLSTM, and MLULCC-ASCS DL systems informed decreased $prec_n$ values of 72.33%, 75.85%, 70.33%, 91.38%, 92%, 94.50%, and 92.99%. Similarly, based on $reca_l$, the GBODL-ALULC technique gains boosted $reca_l$ of 95.05% while the SVM, RF, ANN, LSTM, PSO-mLSTM, HGO-mLSTM, and MLULCC-ASCS DL methods provide minimized $reca_l$ values of 78.80%, 72.30%, 70.51%, 92.91%, 93.98%, 94%, and 92.59%. Also, with F_{score}, the GBODL-ALULC system achieves an improved F_{score} of 95.05% however, the SVM, RF, ANN, LSTM, PSO-mLSTM, HGO-mLSTM, and MLULCC-ASCS DL techniques offer diminished F_{score} values of 77.24%, 73.22%, 73.05%, 92.59%, 92.91%, 92.49%, and 92.81%, correspondingly. Therefore, the GBODL-ALULC technique can be used for effectual LULC classification on SAR data.

5. Conclusion

In this study, we have presented a novel GBODL-ALULC algorithm on SAR data. The GBODL-ALULC technique aims to detect and classify distinct types of land cover that exist in the SAR data. The GBODL-ALULC technique compresses 3 various procedures ResNet-CBAM-based feature extraction, GBO-based hyperparameter tuning, and RELM-based classification process. Initially, the feature extraction process takes place by the ResNet-CBAM approach. At the same time, the GBO algorithm can be performed for the best hyperparameter selection of the ResNet-CBAM model which helps to improve the overall LULC classification

results. At last, the RELM system can be executed for the detection and classification of land covers. The performance analysis of the GBODL-ALULC algorithm is carried out on the SAR dataset. The simulation results demonstrated that the GBODL-ALULC system reaches effectual LULC classification outcomes over compared methods. This approach not only helps businesses adapt to present challenges but also positions them proactively to tackle future complexities, ensuring sustained success and relevance in a dynamically evolving landscape. This technology continues to evolve, the agricultural sector can look forward to even more sophisticated solutions, ensuring food security and sustainable farming for future generations.

Author contributions: Conceptualization, DA and AA; methodology, DA; software, AA; validation, DA, AA and VR; formal analysis, VR; investigation, AA; resources, DA; data curation, DA; writing—original draft preparation, DA; writing—review and editing, AA; visualization, DA; supervision, AA; project administration, VR; funding acquisition, VR. All authors have read and agreed to the published version of the manuscript.

Conflict of interest: The authors declare no conflict of interest.

References

Addison, P., & Oommen, T. (2018). Utilizing satellite radar remote sensing for burn severity estimation. International Journal of Applied Earth Observation and Geoinformation, 73, 292–299. https://doi.org/10.1016/j.jag.2018.07.002

Ajadi, O. A., Barr, J., Liang, S.-Z., et al. (2021). Large-scale crop type and crop area mapping across Brazil using synthetic aperture radar and optical imagery. International Journal of Applied Earth Observation and Geoinformation, 97, 102294. https://doi.org/10.1016/j.jag.2020.102294

Al-Dujaili, M. J. (2024). An accurate algorithm for land surface changes detection based on deep learning and improved pixel clustering using SAR images. Neural Computing and Applications, 36(10), 5545–5554. https://doi.org/10.1007/s00521-023-09377-0

Allies, A., Roumiguié, A., Dejoux, J.-F., et al. (2021). Evaluation of Multiorbital SAR and Multisensor Optical Data for Empirical Estimation of Rapeseed Biophysical Parameters. IEEE Journal of Selected Topics in Applied Earth Observations and Remote Sensing, 14, 7268–7283. https://doi.org/10.1109/jstars.2021.3095537

Arrechea-Castillo, D. A., Solano-Correa, Y. T., Muñoz-Ordóñez, J. F., et al. (2023). Multiclass Land Use and Land Cover Classification of Andean Sub-Basins in Colombia with Sentinel-2 and Deep Learning. Remote Sensing, 15(10), 2521. https://doi.org/10.3390/rs15102521

Asmaa, H. F., Abdelfatah, M. A., Gamal, E. F. (2023). Investigating land use land cover changes and their effects on land surface temperature and urban heat islands in Sharqiyah Governorate, Egypt. The Egyptian Journal of Remote Sensing and Space Science, 26(2), 293–306. https://doi.org/10.1016/j.ejrs.2023.04.001

Bhatt, A., & Thakur, V. (2023). An Optimized Deep Belief Network for Land Cover Classification Using Synthetic-Aperture Radar Images and Landsat Images. The Computer Journal, 66(8), 2043–2058. https://doi.org/10.1093/comjnl/bxac077

Chatterjee, A., Mukherjee, J., Aikat, S., et al. (2020). Semi-supervised Classification of Paddy Fields from Dual Polarized Synthetic Aperture Radar (SAR) images using Deep Learning. International Journal of Remote Sensing, 42(5), 1867–1892. https://doi.org/10.1080/01431161.2020.1846223

Chatterjee, A., Saha, J., Mukherjee, J., et al. (2020). Unsupervised Land Cover Classification of Hybrid and Dual-Polarized Images Using Deep Convolutional Neural Network. IEEE Geoscience and Remote Sensing Letters, 18(6), 969–973. https://doi.org/10.1109/lgrs.2020.2993095

Dahhani, S., Raji, M., Hakdaoui, M., et al. (2022). Land Cover Mapping Using Sentinel-1 Time-Series Data and Machine-Learning Classifiers in Agricultural Sub-Saharan Landscape. Remote Sensing, 15(1), 65. https://doi.org/10.3390/rs15010065

Darvishnezhad, M., & Sebt, M. A. (2023). A novel self-supervised ensemble learning framework for land use and land cover

classification of polarimetric synthetic aperture radar images. IET Radar, Sonar & Navigation, 18(3), 379 – 409. https://doi.org/10.1049/rsn2.12484

Debella-Gilo, M., & Gjertsen, A. K. (2021). Mapping Seasonal Agricultural Land Use Types Using Deep Learning on Sentinel-2 Image Time Series. Remote Sensing, 13(2), 289. https://doi.org/10.3390/rs13020289

Di Martino, T., Guinvarc'h, R., Thirion-Lefevre, L., et al. (2023). FARMSAR: Fixing AgRicultural Mislabels Using Sentinel-1 Time Series and AutoencodeRs. Remote Sensing, 15(1), 35. https://doi.org/10.3390/rs15010035

Fondaj, J., Hamiti, M., Krrabaj, S., et al. (2023). Proposal of Prediction Model for Smart Agriculture Based on IoT Sensor Data. 2023 46th MIPRO ICT and Electronics Convention (MIPRO). https://doi.org/10.23919/mipro57284.2023.10159955

Garg, R., Kumar, A., Prateek, M., et al. (2022). Land cover classification of spaceborne multifrequency SAR and optical multispectral data using machine learning. Advances in Space Research, 69(4), 1726–1742. https://doi.org/10.1016/j.asr.2021.06.028

Ghaffarian, S., Valente, J., van der Voort, M., et al. (2021). Effect of Attention Mechanism in Deep Learning-Based Remote Sensing Image Processing: A Systematic Literature Review. Remote Sensing, 13(15), 2965. https://doi.org/10.3390/rs13152965

Höhl, A., Obadic, I., Torres, M. Á. F., et al. (2024). Opening the Black-Box: A Systematic Review on Explainable AI in Remote Sensing, arXiv:2402.13791.

Hosseiny, B., Abdi, A. M., & Jamali, S. (2022). Urban land use and land cover classification with interpretable machine learning—A case study using Sentinel-2 and auxiliary data. Remote Sensing Applications: Society and Environment, 28, 100843. https://doi.org/10.1016/j.rsase.2022.100843

Hosseiny, B., Mahdianpari, M., Brisco, B., et al. (2022). WetNet: A Spatial–Temporal Ensemble Deep Learning Model for Wetland Classification Using Sentinel-1 and Sentinel-2. IEEE Transactions on Geoscience and Remote Sensing, 60, 1–14. https://doi.org/10.1109/tgrs.2021.3113856

Hosseiny, B., Mahdianpari, M., Hemati, M., et al. (2024). Beyond Supervised Learning in Remote Sensing: A Systematic Review of Deep Learning Approaches. IEEE Journal of Selected Topics in Applied Earth Observations and Remote Sensing, 17, 1035–1052. https://doi.org/10.1109/jstars.2023.3316733

Huang, Y., Meng, M., Hou, Z., et al. (2023). Land Cover Classification of SAR Based on 1DCNN-MRF Model Using Improved Dual-Polarization Radar Vegetation Index. Remote Sensing, 15(13), 3221. https://doi.org/10.3390/rs15133221

Jang, D., Lee, J., & Lee, J. S. (2023). Web-based synthetic-aperture radar data management system and land cover classification. (2023). KSII Transactions on Internet and Information Systems, 17(7). https://doi.org/10.3837/tiis.2023.07.007

Kraatz, S., Torbick, N., Jiao, X., et al. (2021). Comparison between Dense L-Band and C-Band Synthetic Aperture Radar (SAR) Time Series for Crop Area Mapping over a NISAR Calibration-Validation Site. Agronomy, 11(2), 273. https://doi.org/10.3390/agronomy11020273

Lapini, A., Fontanelli, G., Pettinato, S., et al. (2020). Application of Deep Learning to Optical and SAR Images for the Classification of Agricultural Areas in Italy. In: Proceedings of the IGARSS 2020—2020 IEEE International Geoscience and Remote Sensing Symposium. https://doi.org/10.1109/igarss39084.2020.9323190

Li, J., Zhang, X., Yao, Y., et al. (2024). Regularized Extreme Learning Machine Based on Remora Optimization Algorithm for Printed Matter Illumination Correction. IEEE Access, 12, 3718–3735. https://doi.org/10.1109/access.2024.3349421

Manderna, A., Kumar, S., Dohare, U., et al. (2023). Vehicular Network Intrusion Detection Using a Cascaded Deep Learning Approach with Multi-Variant Metaheuristic. Sensors, 23(21), 8772. https://doi.org/10.3390/s23218772

Mitchard, E. T. A., Meir, P., Ryan, C. M., et al. (2013). A novel application of satellite radar data: measuring carbon sequestration and detecting degradation in a community forestry project in Mozambique. Plant Ecology & Diversity, 6(1), 159–170. https://doi.org/10.1080/17550874.2012.695814

Moran, M. S., Peters-Lidard, C. D., Watts, J. M., et al. (2004). Estimating soil moisture at the watershed scale with satellite-based radar and land surface models. Canadian Journal of Remote Sensing, 30(5), 805–826. https://doi.org/10.5589/m04-043

Mucsi, L., & Bui, D. H. (2023). Evaluating the performance of multi-temporal synthetic-aperture radar imagery in land-cover mapping using a forward stepwise selection approach. Remote Sensing Applications: Society and Environment, 30, 100975. https://doi.org/10.1016/j.rsase.2023.100975

Ngo, K. D., Lechner, A. M., & Vu, T. T. (2020). Land cover mapping of the Mekong Delta to support natural resource management with multi-temporal Sentinel-1A synthetic aperture radar imagery. Remote Sensing Applications: Society and Environment, 17, 100272. https://doi.org/10.1016/j.rsase.2019.100272

Niedbała, G., Piekutowska, M., & Hara, P. (2023). New Trends and Challenges in Precision and Digital Agriculture. Agronomy, 13(8), 2136. https://doi.org/10.3390/agronomy13082136

Sameh, S., Zarzoura, F. H., & El-Mewafi, M. (2023). Spatiotemporal analysis of Urban Heat Island and land use land cover changes using Landsat images and CA-ANN machine learning techniques: a case study of Dakahlia government, Egypt. Journal of Spatial Science, 1–22. https://doi.org/10.1080/14498596.2023.2257619

Sameh, S., Zarzoura, F., & El-Mewafi, M. (2022). Automated Mapping of Urban Heat Island to Predict Land Surface Temperature and Land use/cover Change Using Machine Learning Algorithms: Mansoura City. International Journal of Geoinformatics, 18(6), 47–67.

Sánchez-Crespo, F. A., Gómez-Villarino, M. T., Gallego, E., et al. (2023). Monitoring of Water and Tillage Soil Erosion in Agricultural Basins, a Comparison of Measurements Acquired by Differential Interferometric Analysis of Sentinel TopSAR Images and a Terrestrial LIDAR System. Land, 12(2), 408. https://doi.org/10.3390/land12020408

Šćepanović, S., Antropov, O., Laurila, P., et al. (2021). Wide-Area Land Cover Mapping with Sentinel-1 Imagery Using Deep Learning Semantic Segmentation Models. IEEE Journal of Selected Topics in Applied Earth Observations and Remote Sensing, 14, 10357–10374. https://doi.org/10.1109/jstars.2021.3116094

Solórzano, J. V., Mas, J. F., Gao, Y., et al. (2021). Land Use Land Cover Classification with U-Net: Advantages of Combining Sentinel-1 and Sentinel-2 Imagery. Remote Sensing, 13(18), 3600. https://doi.org/10.3390/rs13183600

Stabel, E., & Fischer, P. (2001). Satellite radar interferometric products for the urban application domain. Advances in Environmental Research, 5(4), 425–433.

Stateczny, A., Bolugallu, S. M., Divakarachari, P. B., et al. (2022). Multiplicative Long Short-Term Memory with Improved Mayfly Optimization for LULC Classification. Remote Sensing, 14(19), 4837. https://doi.org/10.3390/rs14194837

Vali, A., Comai, S., & Matteucci, M. (2020). Deep Learning for Land Use and Land Cover Classification Based on Hyperspectral and Multispectral Earth Observation Data: A Review. Remote Sensing, 12(15), 2495. https://doi.org/10.3390/rs12152495

Wang, H., & Zhang, X. (2024). Fault Diagnosis Using Imbalanced Data of Rolling Bearings Based on a Deep Migration Model. IEEE Access, 12, 5517–5533. https://doi.org/10.1109/access.2024.3350785

Wu, X., Hong, D., & Chanussot, J. (2022). Convolutional Neural Networks for Multimodal Remote Sensing Data Classification. IEEE Transactions on Geoscience and Remote Sensing, 60, 1–10. https://doi.org/10.1109/tgrs.2021.3124913